PCCP

PAPER

View Article Online
View Journal | View Issue

Cite this: *Phys. Chem. Chem. Phys.*, 2021, **23**, 22133

Electrical properties and charge compensation mechanisms of Cr-doped rutile, TiO_2†

Yun Dang, [a] Xin Li Phuah, [b] Han Wang,[b] Bo Yang, [b] Haiyan Wang [bc] and Anthony R. West *[a]

Received 21st April 2021,
Accepted 15th September 2021

DOI: 10.1039/d1cp01735g

rsc.li/pccp

Cr-doped rutile, $Ti_{1-x}Cr_xO_{2-x/2-\delta}$, powders and ceramics with $0 \leq x \leq 0.05$ were prepared by solid state reaction and sintered at 1350 °C. Cr distribution is homogeneous with no evidence of either segregation or crystallographic shear plane formation. For high x compositions, $> \sim 0.01$, Cr substitution is charge-compensated ionically by oxygen vacancies with two Cr^{3+} ions for each vacancy and the materials are electronically insulating. For low x compositions, the materials are semiconducting. This is attributed to a new charge compensation mechanism involving Ti^{3+} ions created in response to the local electroneutrality requirement for two trivalent cations to be in close proximity to each oxygen vacancy. At very low dopant concentrations, $\ll 0.01$, the dopants are well-separated and instead, some Ti^{3+} ions act as a second dopant to preserve local electroneutrality. For intermediate x compositions, a core–shell structure is proposed consisting of semiconducting grain interiors containing Ti^{3+} ions surrounded by a more insulating shell with Cr^{3+} ions as the only acceptor dopant. Lattice parameters show unusual, non-linear Vegard's law behaviour characterised by a maximum in cell volume at intermediate $x \sim 0.005$, that is attributed to the composition-dependent presence of Ti^{3+} ions.

1 Introduction

Rutile, TiO_2 is an important functional material that has a wide variety of applications associated with its electrical properties which range from insulating to semiconducting, depending on dopants and defect structure. The thermodynamics of point defect equilibria in pure and doped rutile are well-documented[1–3] but in addition, extended defects are present in many materials associated with crystallographic shear (CS) planes and their ordered arrangements in the homologous series of Magnéli phases.[4–6]

TiO_2 loses a small amount of oxygen spontaneously at high temperatures and this deficiency may either be preserved by quenching or eliminated by annealing at lower temperatures.[7] Consequently, the electrical properties at room temperature depend very much on sample processing history, particularly the temperature and atmosphere during heating and the subsequent cooling rate.[7,8] The lattice parameters at room temperature of quenched oxygen-deficient rutile show markedly non-linear Vegard's law behaviour.[9] A change from chemical expansion to chemical contraction occurs with increasing oxygen loss. The reasons for this are not well-understood but may be associated with the formation of CS planes with increased oxygen deficiency.[4,9]

The aim of the present work was to determine how the electrical properties of rutile change in materials that have Cr^{3+} added as an acceptor (lower valency) dopant. If charge compensation is by means of oxygen vacancy creation, then insulating behaviour, with the possibility of some oxide ion conduction may be expected. If additional oxygen loss occurs during high temperature synthesis, then n-type electronic conductivity may be expected. Charge compensation for acceptor dopants sometimes involves hole creation and associated p-type electronic conduction is a possibility if oxygen atoms in the rutile lattice are redox-active. Also, the resulting structures may be electrically heterogeneous or homogeneous depending on the distribution of dopants and oxygen vacancies.

At present, there is little information in the literature on how electrical properties change on addition of an acceptor dopant such as Cr^{3+} and/or as a consequence of different processing conditions. Here, we use impedance spectroscopy to investigate the electrical properties and electrical homogeneity of samples; by also making measurements in atmospheres of different oxygen partial pressure, pO_2, we gain information on the nature of conducting species, the doping mechanisms and associated defect structures. This is complemented by transmission

[a] *University of Sheffield, Department of Materials Science & Engineering, Sheffield S1 3JD, UK. E-mail: a.r.west@sheffield.ac.uk*
[b] *Purdue University, School of Materials Engineering, West Lafayette, IN, 47907, USA*
[c] *Purdue University, School of Electrical and Computer Engineering, West Lafayette, IN, 47907, USA*

† Electronic supplementary information (ESI) available. See DOI: 10.1039/d1cp01735g

electron microscopy to look for the presence of CS planes and determine the homogeneity of Cr dopant distribution.

2 Experimental

Samples of $Ti_{1-x}Cr_xO_{2-x/2-\delta}$ (x = 0, 0.0002, 0.001, 0.002, 0.004, 0.005, 0.006, 0.008, 0.01, 0.015, 0.02, 0.03 and 0.05) were prepared by solid state reaction using TiO_2 (Sigma-Aldrich, 99.9%) and Cr_2O_3 (Johnson Matthey, 99%) which were dried prior to weighing at 900 °C and 600 °C, respectively. These were mixed in small quantities (1–2 g) in a mortar and pestle for ~30 min, with acetone added periodically to form a paste. For most compositions, sample size was 1–2 g, but for those with smallest Cr content, samples up to 10 g were prepared and contained at least 1 mg Cr_2O_3 which was weighed out using a balance with 0.1 mg sensitivity. The possible impurities in the Cr_2O_3 reagent were the oxides of Al, Fe, Ca and Na with a total concentration of <1% of the Cr_2O_3 content. On reaction with TiO_2, they may all be regarded as lower valence acceptors, similar to Cr. They would, therefore, be expected to have a similar effect to Cr on the doping mechanisms and associated electrical properties of TiO_2 but to a much lesser extent because their concentration was <1% of the Cr content in each composition.

The dried powders were heated in Pt boats at 1350 °C for 8 h in air, followed by a slow cool (5 °C min^{-1}) inside the furnace. For electron microscopy and electrical property measurements, pellets (10 mm diameter and 1–2 mm thick) were prepared by either uniaxial pressing or cold isostatic pressing and fired at 1350 °C for 8 h to give a final density of ~90%.

Powder X-ray Diffraction (PXRD) used a Siemens D5000 Diffractometer with a linear position-sensitive detector. Lattice parameters were determined by least-squares refinement for reflections in the range $10 < 2\theta < 80°$, using the software WinXPow version 2.10, and an internal Si standard. For electron microscopy, pellets were sectioned, mechanically ground and dimpled, followed by ion polishing in a precision ion milling system (PIPS II, Gatan) to give electron transparency. Transmission electron microscopy (TEM) was performed on an FEI TALOS F200X TEM/STEM with ChemiSTEM technology (X-FEG and SuperX EDS with four silicon drift detectors) at 200 kV.

For electrical property measurements, electrodes were fabricated on opposite pellet faces using Pt paste that was decomposed and hardened by heating to 900 °C for 2 h. Samples with electrodes attached were placed in a conductivity jig inside a horizontal tube furnace. Impedance measurements were made in either air, N_2 or O_2 using a combination of Modulelab XM Solartron and Solartron SI 1260 instrumentation over the frequency range 0.1 Hz to 1 MHz with an ac measuring voltage of 100 mV. For measurements in N_2, the pO_2 inside the conductivity rig was not measured but was estimated to be in the range 10^{-2} to 10^{-3} atm O_2. Impedance data were corrected for overall pellet geometry and resistance values are reported in units of Ohm cm. Bulk resistivities correspond fairly well to measured sample resistances, therefore, but no additional geometrical correction was applied to the grain boundary resistance data to convert them to grain boundary resistivities. Data were also corrected for the blank capacitance of the empty conductivity jig and the inductance of the leads measured with the jig on closed circuit.

Oxide ion transport numbers were estimated using a Probostat system. A 20 mm-diameter pellet made by uniaxial pressing at 50 MPa followed by cold isostatic pressing at 200 MPa was sintered, coated with Pt electrodes on both sides and sealed over the end of an open, yttria stabilised zirconia, YSZ tube by a glass frit. The YSZ tube also had Pt contacts on both sides to act as a pO_2 sensor and to confirm the leak-free nature of the experimental set-up. The atmosphere outside the YSZ tube was air with flowing O_2 inside the tube. The voltage between inner and outer sample electrodes was measured and compared with the voltage across the YSZ tube to estimate the oxide ion transport number. Voltages were measured by a Keithley 175 Autoranging Multimeter in the range 600 to 800 °C.

3 Results and discussion

3.1 X-ray diffraction, TEM and possible doping mechanisms

3.1.1 X-ray diffraction. Samples of Cr-doped TiO_2 of general formula $Ti_{1-x}Cr_xO_{2-x/2-\delta}$, reacted at 1350 °C for 8 h and cooled in the furnace at 5 °C min^{-1}, were a green colour at very low x, 0.0002 and 0.001, but became increasing black at higher x. Samples with composition $0 \leq x \leq 0.05$ were single phase by PXRD and indexed on the tetragonal unit cell of the rutile structure, Fig. 1. Formation of a rutile solid solution is consistent with literature data on the phase diagram of the TiO_2–Cr_2O_3 system. Several phase diagrams are reported:[10–13] all agree that a rutile solid solution forms with a solid solution limit of x = *ca.* 0.06, which may be slightly temperature-dependent. At higher Cr content, a series of Magnéli phases of general formula $Ti_{n-2}Cr_2O_{2n-1}$ forms with specific single-phase compositions at n = 6, 7, 8, 9.[6,10,13]

Unit cell parameters obtained by least squares refinement of the d-spacings of the first 11 lines are shown in Fig. 1(b–d) as a function of x. For the composition range $0 \leq x \leq 0.05$, a increases, c decreases and the cell volume passes through a maximum at x = *ca.* 0.005. This non-linear behaviour is very different from the linear Vegard's Law response typically seen in oxide solid solutions but is somewhat similar to that reported previously for undoped rutile, $TiO_{2-\delta}$ quenched from different temperatures.[9] (Those samples had different degrees of oxygen deficiency δ; the cell parameters and cell volume all passed through maxima at intermediate values of δ[9]). Data in Fig. 1(d) show a small overall increase in volume between x = 0 and x = 0.05; superposed on this is the maximum at intermediate compositions peaking around x = 0.005.

3.1.2 TEM. TEM was carried out on a sample of x = 0.006, primarily to determine the Cr distribution and look for the presence of any planar defects. The bright-field TEM image for x = 0.006 is shown in Fig. 2(a). No planar faults were observed, consistent with the results of Gibb and Anderson[6] who did not

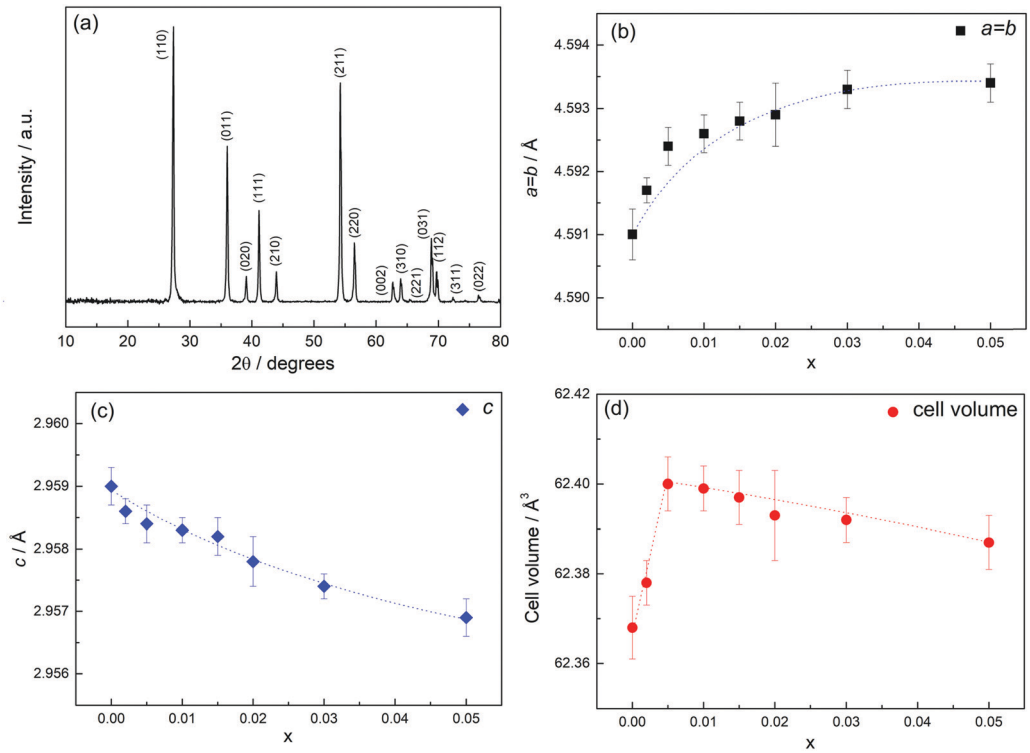

Fig. 1 (a) PXRD pattern of composition x = 0.01 sintered in air followed by slow cooling, (b–d) lattice parameters and cell volume against x.

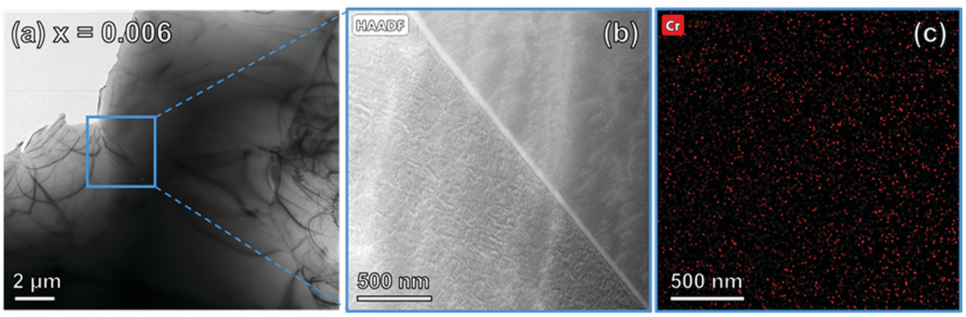

Fig. 2 (a) Bright-field TEM image of sample x = 0.006. (b) STEM image under HAADF conditions of a grain boundary and the corresponding Cr elemental mapping in (c).

detect CS planes in compositions up to x = 0.05. The reported Magnéli phases with ordered CS planes in Cr-doped rutile have much higher Cr content than the solid solutions studied here. It is possible that, under different sample processing conditions, such as in a reducing atmosphere, CS planes may form as random planar defects at lower values of x, but no evidence for this possibility was found in the present study.

Fig. 2(b) shows the scanning transmission electron microscopy (STEM) image under high angle annular dark-field (HAADF) conditions and the corresponding Cr elemental mapping in Fig. 2(c). The Cr distribution throughout the grains was homogeneous and continuous across grain boundaries with no evidence of depletion or accumulation. This showed that the reaction conditions yielded products with a uniform cation distribution. It is highly likely, therefore, that samples were in thermodynamic equilibrium at the sintering temperature.

The homogeneity of the Cr distribution shown in Fig. 2(c) would perhaps be remarkable if it occurred by a mechanism dominated by slow, solid state inter-diffusion processes. However, a vapour phase transport mechanism may have been responsible in which the transporting agent was volatile CrO_3, formed by reaction of Cr_2O_3 with O_2. Such a mechanism was proposed for the reaction of NiO and Cr_2O_3 to form $NiCr_2O_4$.[14]

3.1.3 Possible doping mechanisms. In order to interpret the lattice parameter results, we consider first the possible charge compensation mechanisms associated with aliovalent doping of TiO_2 by Cr^{3+}. These considerations are also critically important for understanding the effect of composition on the

electrical properties, discussed later. The main defects of concern in Cr-doped rutile are oxygen vacancies (assumed to be doubly-charged $V_O^{\bullet\bullet}$ in Kroger–Vink notation), electrons and holes, for which the overall electro-neutrality condition is:

$$2[V_O^{\bullet\bullet}] + [h^{\bullet}] = [Cr'] + [e'] \quad (1)$$

In order to understand the properties of Cr-doped TiO_2, it is necessary to understand the variables that affect the amount of each defect type.

The simplest ionic compensation mechanism on substitution of Ti^{4+} by Cr^{3+} on the octahedral sites would involve oxygen vacancy creation with the formula:

$$Ti_{1-x}Cr_xO_{2-x/2} \quad (2)$$

The oxygen vacancies that are created may give rise to oxide ion conduction and there is no change in the valence state of the cations. Oxygen vacancy creation could also be caused by loss of oxygen from the samples. Oxygen loss occurs at high temperature in un-doped TiO_2 and can be represented by the formula:

$$Ti_{1-2\delta}{}^{4+}Ti_{2\delta}{}^{3+}O_{2-\delta} \quad (3)$$

leading to a large increase in n-type electronic conductivity that is attributed to the mixed valence of Ti.[7] If oxygen loss according to (3) occurs in Cr-doped samples, in addition to that associated with ionic compensation in (2), this would correspond to the more general formula:

$$Ti_{1-x-2\delta}{}^{4+}Cr_x{}^{3+}Ti_{2\delta}{}^{3+}O_{2-x/2-\delta} \quad (4)$$

Mechanism (2) has the practical constraint that, in order to preserve local electro-neutrality, each oxygen vacancy requires the presence of two substitutional Cr^{3+} ions close to the vacancy. An alternative viewpoint to formula (4) is, therefore, to regard it as representing double doping TiO_2 by two acceptors, Cr^{3+} and Ti^{3+}, in relative amounts determined by the values of x, which is given by the overall cation composition and δ, which depends on processing conditions and sample history. Under standard conditions of synthesis in air, reduction of Ti^{4+} to Ti^{3+} is not expected to occur, unless the sample loses a small amount of oxygen spontaneously at high temperatures, as in (3). In Cr-doped TiO_2, however, as discussed later, compositions with very low Cr content are semiconducting, which appears to imply the presence of Ti^{3+} ions. The driving force for creation of Ti^{3+} ions is linked to the necessity to have two substitutional trivalent ions, Cr^{3+} and/or Ti^{3+}, locally, for every oxygen vacancy. Statistically, close proximity of two Cr^{3+} ions is unlikely at very low doping levels and instead, Ti^{3+} is incorporated as a second acceptor in addition to Cr^{3+}. The amount of Ti^{3+} created in this way is dependent on the Cr content and is temperature-independent, in contrast to that associated with high temperature oxygen loss which is very temperature-dependent. Ti^{3+} is responsible for both the electron content and a considerable fraction of the oxygen vacancy content, both of which may be much greater than that associated with spontaneous oxygen loss at high temperatures. Depending on experimental conditions, formula (4) covers all possible combinations of (2) and (3). Both mechanisms may occur simultaneously for low x values, with ideally $\delta = 2x$, but a gradual shift to (2) is anticipated with increasing x.

An additional electronic mechanism of charge compensation for the acceptor dopant Cr^{3+} is the possibility of hole creation. If the holes are localised on an atomic species rather than delocalised in a conduction band, the possible locations are on: (i) Ti^{4+}, (ii) Cr^{3+}, (iii) O^{2-}, (iv) unidentified impurity cations. As discussed later, we find evidence for p-type conductivity in some compositions and believe that (iii) is the only realistic possibility for location of holes in the present materials. A general formula that involves holes on oxygen, ideally as O^- ions, is:

$$Ti_{1-y}{}^{4+}Cr_y{}^{3+}O_{2-y}{}^{2-}O_y{}^{-} \quad (5)$$

However, this does not involve oxygen vacancy creation to compensate for the substitution of Cr^{3+} and indeed, would require oxygen uptake by the TiO_2/Cr_2O_3 reaction mixture. A second possibility is internal redox electron transfer:

$$O^{2-} + Ti^{4+} \leftrightarrow O^- + Ti^{3+} \quad (6)$$

which would potentially, give rise to two mobile electronic species, electrons and holes; it could be facilitated by a local defect structure in which oxygen ions were under-bonded and ionised spontaneously. A third possibility, for which there is direct experimental evidence, discussed later, involves the absorption, dissociation and ionisation of atmospheric oxygen. Assuming for simplicity that (i) O^- ions are the main species for hole location, (ii) pre-existing oxygen vacancies are present and (iii) oxide ions adjacent to the vacancies can ionise, holes on oxygen may be created by oxygen absorption according to the schematic reaction:

$$V_O + \frac{1}{2}O_2 + O^{2-} \leftrightarrow 2O^- \quad (7)$$

This means that an adsorbed O_2 molecule dissociates and each oxygen atom picks up one electron from an adjacent lattice O^{2-} ion, to form two O^- ions. Mechanism (7) establishes a link with the simultaneous occurrence of ionic charge compensation mechanism (2) which involves oxygen vacancy creation and provides lattice sites for adsorption of oxygen species.

The reason why a lattice oxide O^{2-} ion may ionise readily to form O^- is attributed to the under-bonding that results on substitution of an adjacent Ti^{4+} ion by a lower valence acceptor, *i.e.*, Ti^{3+} or Cr^{3+}, as discussed for creation of p-type conductivity in acceptor-doped $BaTiO_3$.[15,16] Oxide ions at sample surfaces and interfaces may also be similarly under-bonded because they are not surrounded by the full complement of positive charge required for local electro-neutrality.

We see no evidence for the need to consider that Cr may change its valence in the doped materials, especially to create Cr^{4+}. CrO_2 itself has the rutile structure and has a high electronic conductivity but its synthesis requires oxidising conditions and it is not thermally stable. The composition-dependence of electrical properties would not be explained readily by the presence of Cr^{4+}dopant.

We had considered, initially, the possibility that CS plane formation may have been responsible for the reduction in cell volume for $x > \sim 0.005$, Fig. 1(d). The absence of CS planes in the TEM results enables us to discount this possibility and therefore, to exclude CS plane formation from consideration of possible doping mechanisms and defect formation. We consider that the anomalous change in lattice parameters, Fig. 1, involves initially a lattice expansion as Ti^{3+} ions are created in response to the need to preserve local electroneutrality. As the Cr^{3+} content increases further, there is less need for the double doping mechanism of charge compensation and as $\delta \rightarrow 0$ with increasing x, the Ti^{3+} content also decreases to zero. Octahedral Cr^{3+} ions are of similar size to Ti^{4+}; the creation of O^- ions may involve a small reduction in cell volume since O^- ions are likely to be smaller than O^{2-} ions. Since Ti^{4+} ions are substituted exclusively by Cr^{3+} at larger x values, together with the creation of oxygen vacancies, an overall reduction in electrostatic attraction and (Ti,Cr)–O bond strength is expected and may explain the small increase in cell volume between $x = 0$ and $x = 0.05$ shown in Fig. 1(d), superposed on which is the maximum associated with the presence of Ti^{3+} ions at intermediate values of x.

An additional factor that may affect the compositional dependence of lattice parameters is the formation of defect complexes. Two broad categories of departure from linear Vegard's Law behaviour involve either a tendency to defect clustering and a net reduction in cell parameters or a tendency to phase separation leading to an effective increase in cell parameters.[17] A well-studied example of the first category is Gd-doped CeO_2 with the fluorite structure, for which defect clustering at high Gd contents leads to smaller cell parameters than those expected for a random defect distribution.[18,19] In Cr-doped TiO_2, while the presence of Ti^{3+} ions is thought to be the main cause of anomalous cell parameter changes at low x, other factors such as cluster formation by the association of oppositely charged defects and/or the apparent two-phase nature of a range of low x compositions, may complicate the overall composition- dependence of the cell parameters and also influence the concentration of mobile charge carriers.

3.2 Impedance data

Impedance data were collected for 13 compositions with x values in the range $0 \leq x \leq 0.05$. Most measurements were made in air over the temperature range 25 to 550 °C. The data fall into two groups, $0 \leq x \leq 0.008$ (low x) and $0.01 \leq x \leq 0.05$ (high x). A typical set of data for each, with $x = 0.002$ and 0.03, is shown in Fig. 4 and 6; representative data for all samples and temperatures are given in ESI,† Fig. S1–S11.

Initial evaluation of all data sets showed them to be consistent with the idealised master circuit shown in Fig. 3 that contains four components in series, although all four components were never observed simultaneously in a given data set. For low x samples, this was due to limitations of the available frequency range, 0.1 to 10^6 Hz, whereas for high x samples, not all components appeared to be present. For accurate fitting of the data, it was necessary to add one or more constant phase element, CPE, to the parallel RC elements representing each component, as discussed later. To aid presentation of the data and discussion of the results, we first describe some general features of the data and draw initial conclusions.

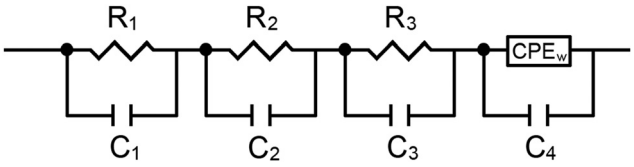

Fig. 3 Equivalent circuit used to model the impedance data.

The four components were characterised by their capacitance values with $C_1 < C_2 < C_3 < C_4$ from which, the initial assignments made were as follows. C_1 and C_2 appear to be bulk components with volume fractions dependent on overall composition. C_3 appears to be a typical grain boundary capacitance. C_4 is a sample–electrode contact capacitance. Each component can be represented in the first instance by an ideal, parallel RC element and these are connected in series in Fig. 3.

A useful parameter in data analysis is the time constant, τ, of each component, given by the RC product, $\tau = RC$. τ is an intrinsic property of an RC element since it is independent of the geometry and dimensions of the region responsible, *i.e.*, $\tau = RC = \rho\varepsilon$, where ρ and ε are the resistivity and permittivity of the region. This means that, for instance, all the electrically homogeneous grains in a ceramic material would have the same τ value, independent of any variation in grain size. For convenience, we label the four components by their τ values, τ_1 to τ_4.

Impedance data can be presented in four complex formalisms: impedance, Z^*, modulus, M^*, admittance, Y^* (or A^*) and permittivity, ε^*,[20] which are inter-related by:

$$Z^* = (Y^*)^{-1} \quad (8)$$

$$M^* = j\omega C_0 Z^* \quad (9)$$

$$\varepsilon^* = (M^*)^{-1} \quad (10)$$

$$Y^* = j\omega C_0 \varepsilon^* \quad (11)$$

Data can be presented either as complex plane plots, *i.e.* imaginary *vs.* real components, usually on linear scales, also known as Nyquist plots, or as spectroscopic plots of one component against frequency, usually on logarithmic scales, also known as Bode plots. Which presentations to use is a matter of personal choice and largely depends on the information that is required, but it is not usually necessary to use all four formalisms and presentation types.

3.2.1 Low x compositions, $0 \leq x \leq 0.008$. Composition $x = 0.002$, Fig. 4, gave impedance data typical of those in the low x range and which are interpreted using the circuit given in Fig. 3. To extract the maximum amount of information on the electrical make-up of the sample, the following strategy is used. First, the same sets of impedance data are presented in four complementary ways since visual inspection of the plots allows the most appropriate equivalent circuit to be identified: different plots emphasise different features of the equivalent

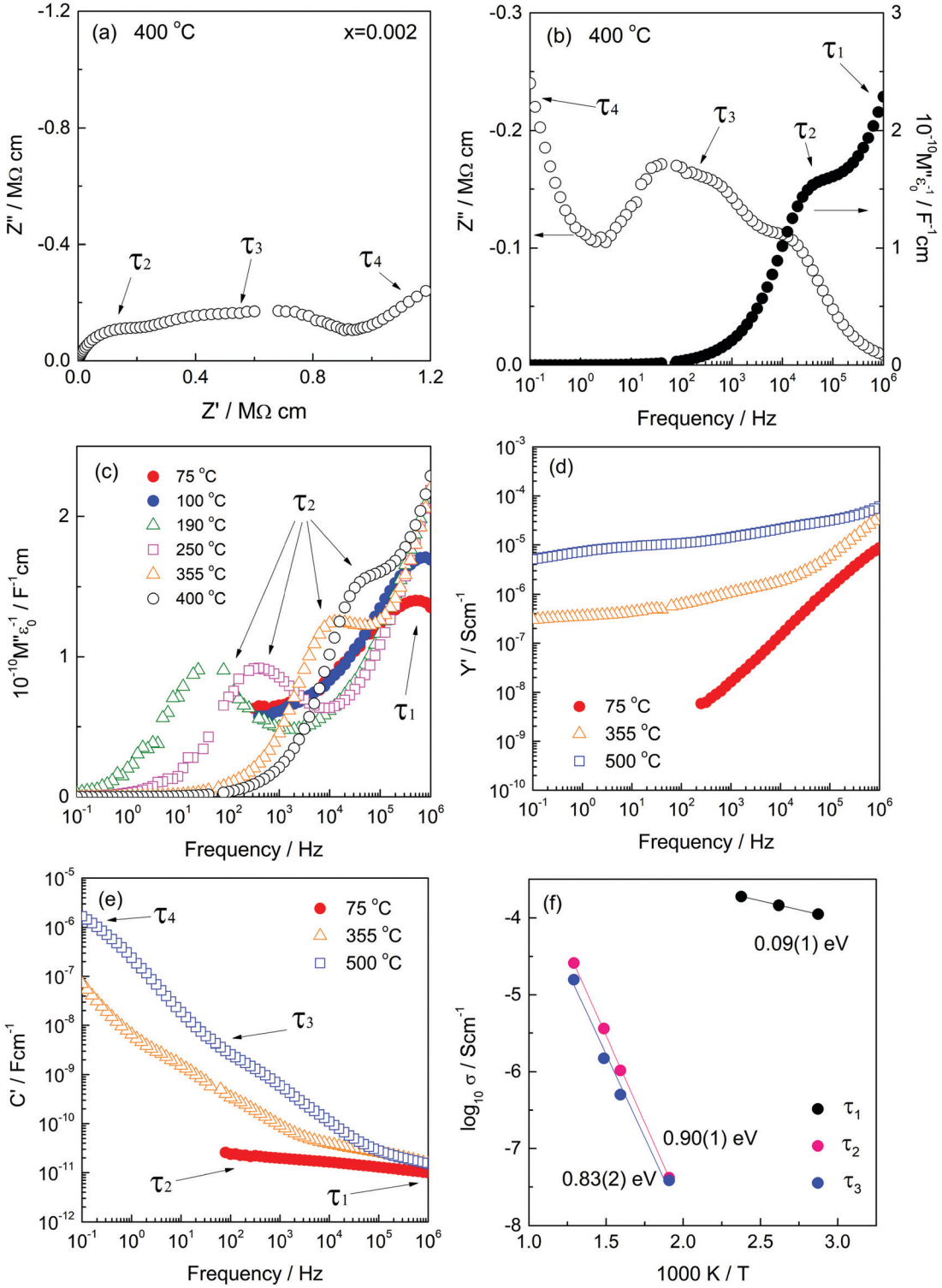

Fig. 4 Impedance data for composition x = 0.002: (a) impedance complex plane plots Z^*, (b and c) spectroscopic plots of Z''/M'', (d) Y' plots, (e) C' plots and (f) Arrhenius plots of conductivity for τ_1–τ_3.

circuit due to the various weighting factors implicit in the plots, which also includes use of either linear or logarithmic scales for data presentation. Second, in order to extract component R and C parameter values, it is necessary to establish the correct equivalent circuit since the equations that are used depend implicitly on the circuit chosen. Third, if necessary, circuit fitting can be carried out to extract precise parameter values and estimate the quality of fit between the proposed equivalent circuit and experimental data. An illustrative discussion of the analysis of data for a sample of one composition, x = 0.002, is as follows:

The impedance complex plane plot, Z^*, Fig. 4(a), shows three features with two broad, overlapping arcs at higher frequencies and an inclined spike at the lowest frequencies; these are attributed to components τ_2 to τ_4. Evidence for a fourth component τ_1 is seen in the M'' plot (b) at highest frequencies. Data are shown at 400 °C and include all the features seen at other temperatures. C' plots (e) show plateaux, often poorly-resolved, from which capacitance values can be obtained and assignments to sample characteristics made. Thus, the low frequency spike in (a) with capacitance >1 μF is attributed to the sample–electrode impedance, τ_4. The lower frequency arc in (a) with capacitance ~2–3 nF, (e), is attributed to the grain boundary impedance, τ_3. The higher frequency arc with capacitance ~50 pF, is attributed to a minor bulk component, τ_2. The main bulk component, τ_1, is hidden in the Z^* complex plane plot close to the origin in (a) since the value of R_1 is several orders of magnitude smaller than R_2 and R_3, (f), but is seen in the corresponding M'' plot (b). Element τ_1 has the smallest capacitance and is attributed to highly conducting grain cores. The total sample resistance, $(R_1 + R_2 + R_3)$, is given by the intercept of either the combination of arcs at low frequencies, or the spike, on the Z' axis.

M'' plots for a selection of temperatures are shown in (c); the peak maximum for τ_1 is seen at the lowest temperatures, but this moves off-scale with increasing temperature at the same time as the peak maximum for τ_2 appears on-scale at lower frequencies. There is no evidence of peak τ_1 in either the Z'' or Z^* plots because its resistance is too small to be seen clearly on the linear Z'/Z'' scales that are used, but the peak for τ_2 is seen at similar frequencies in both Z'' and M'' plots (b). In summary, all four components are seen in the combined M''/Z'' plots: the high capacitance components τ_3 and τ_4 are too small to see in M'' whereas the high conductivity component, τ_1 is too small to see in Z'' and Z^*.

Plots of $\log Y'$ *vs.* $\log f$, (d), support these conclusions. They give a wide, poorly-defined plateau for τ_2 and/or τ_3 at 355 and 500 °C; at 75 °C, a large high frequency dispersion towards much higher conductivity values dominates the presentation, leading to the likelihood of a high frequency plateau associated with τ_1 that is off-scale. The implication from this, and the high frequency peaks in M'' plots, is that the sample grains contain a conductive core, τ_1, in series with more resistive components τ_2 and/or τ_3.

The C' spectroscopic plots (e) show the same four main features τ_1 to τ_4 and their magnitudes help greatly in assigning them to sample characteristics. The broad low frequency dispersion in C' levels off at still lower frequencies, as shown more clearly for $x = 0.001$ in Fig. S3(d) (ESI†), and is a characteristic feature of a blocking capacitance associated with oxide ion conduction. The inflexion around 2–3 nF is attributed to a grain boundary capacitance, τ_3. The plateau around 40 pF, attributed to τ_2 and seen most clearly at 355 °C, is too small to be a typical grain boundary component and instead, is attributed to a secondary bulk component. The gradual decrease at highest frequencies with a limiting capacitance of ~8 pF seen at 75 °C and more clearly for $x = 0.005$ in Fig. S5(d) (ESI†), is attributed to τ_1, the main bulk component.

The data sets in the low x range $0.0002 \leq x \leq 0.008$, including Fig. 4, are unusual in showing evidence of two frequency-independent regions that have small capacitance values: ~8 pF (C_1) and ~40 pF (C_2) for $x = 0.002$, but whose values change with x. Such low values are typical of components that occupy a large volume fraction of the sample. A value of 8 pF, corresponds to a permittivity of ~90 (from the relation $\varepsilon' = C/e_0$, where e_0 is the permittivity of free space, 8.854×10^{-14} F cm^{-1}) and is typical of rutile-based materials. τ_1 therefore, is the main bulk component. For composition $x = 0.002$, the value of component C_2 represents a second bulk component, τ_2 that occupies approximately 20% of the sample volume.

Both components C_1 and C_2 are seen in low x compositions and capacitance C_1 increases at the same time that C_2 decreases with increasing x. This is shown by the change in relative heights of the two M'' peaks, Fig. 5, that represent τ_1 and τ_2

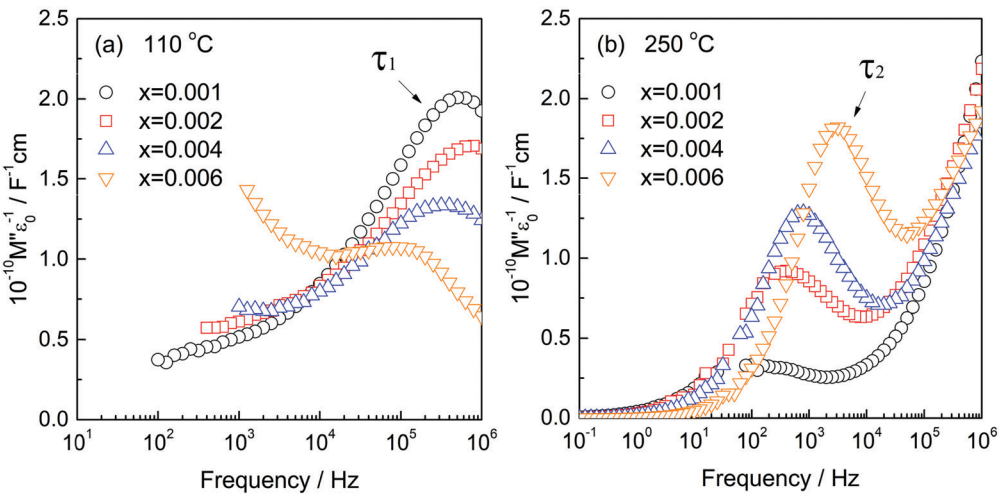

Fig. 5 M'' spectroscopic plots for $x = 0.001$, 0.002, 0.004 and 0.006 at (a) 110 °C and (b) 250 °C.

and have an opposite dependence of peak height on composition, x. Specifically, peak τ_1 is the main peak at low x, 0.001, (a) but is gradually replaced by peak τ_2 as the composition increases to x = 0.006, (b). M'' peak height depends inversely on capacitance (for an ideal parallel RC element, $M_{max}'' = e_0/2\varepsilon'$) and therefore, is approximately proportional to volume fraction. We conclude from Fig. 5 that component τ_1 has a composition $x < 0.001$ which is very close to that of undoped rutile but contains an essential, small amount of Cr dopant. Component τ_2 has a composition estimated as x = 0.009(1), which corresponds to replacement of <1% Ti by Cr. The resistances of components τ_1 and τ_2 have very different activation energies, as shown in Fig. 4(f); resistances were obtained from the frequency maxima of M'' spectroscopic plots at which, ideally, the relation $2\pi fRC = 1$ holds. R_1 has a small activation energy, 0.09(1) eV, consistent with the much higher conductivity of region τ_1. Further discussion of activation energies and conductivities of all compositions is discussed later.

Electrically, therefore, low x compositions appear to be two-phase. By contrast, high x compositions appear to be single phase: C' data show evidence for only a single bulk capacitance in high x compositions, $x \geq 0.01$, Fig. 6, discussed next.

3.2.2 High x compositions, $0.01 \leq x \leq 0.05$. A typical impedance data set for one composition, x = 0.03, is shown in Fig. 6. The data are very much simpler than those for low x compositions and have the following characteristics: (a) a single arc in Z^* plots; (b) single, almost overlapping peaks in M''/Z'' spectra; (c) a high frequency plateau in C' with value ~6 pF and a small low frequency dispersion associated with a CPE; (d) a conductivity plateau in Y' and a high frequency dispersion associated also with the CPE. The data correspond therefore to a single bulk response consisting of a resistor, capacitor and a CPE in parallel. For consistency with the results on low x compositions, we label this component as τ_2 since, from Fig. 5, τ_1 decreases and τ_2 increases in volume fraction with increasing x and τ_1 is not seen at all in high x compositions.

3.2.3 Identification of the charge carrier species. We use three sets of results to gather information on the nature of the current carrying species. First, low frequency impedance data with high capacitance values in the microfarad range provide an indication of ionic conductivity. Second,

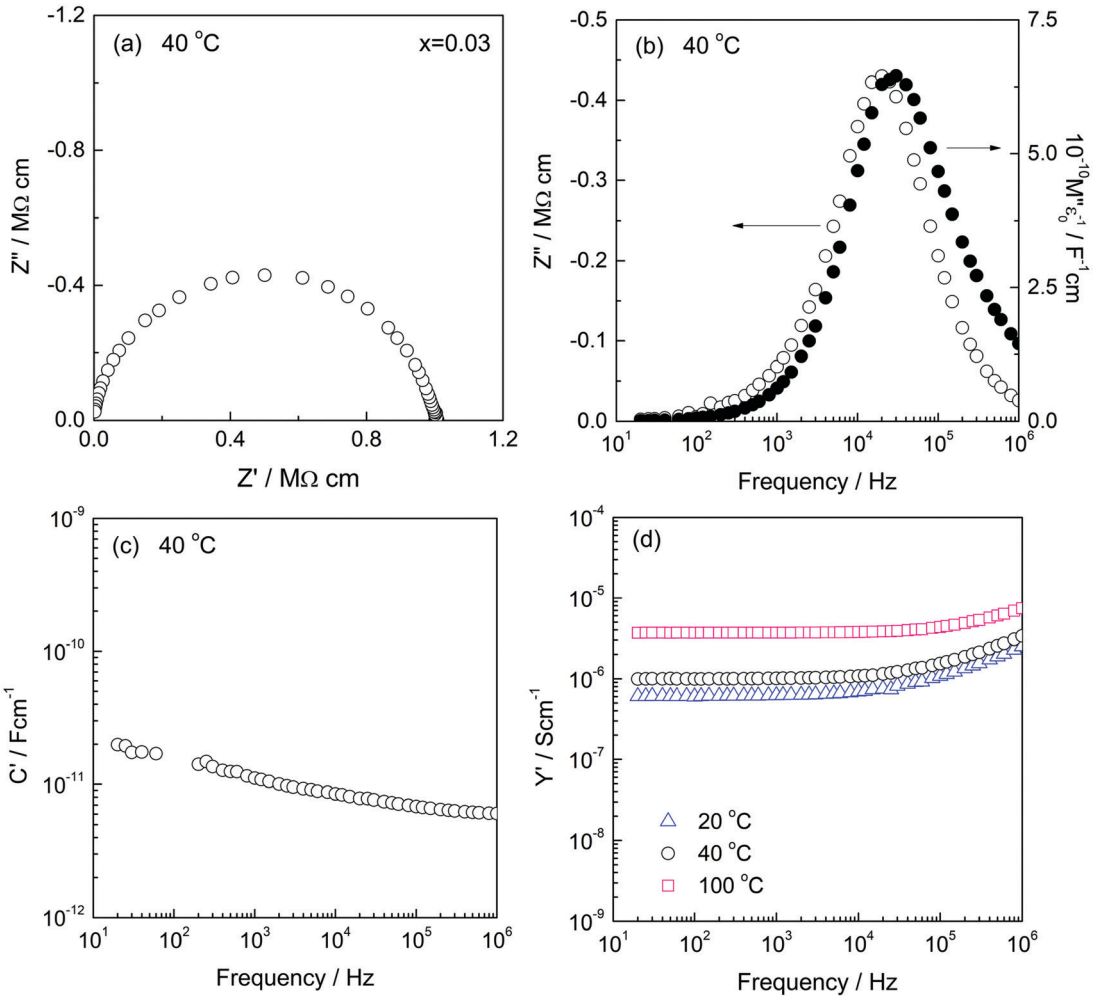

Fig. 6 Impedance data for composition x = 0.03: (a) impedance complex plane plots Z^*, (b) Z''/M'', (c) C' and (d) Y'.

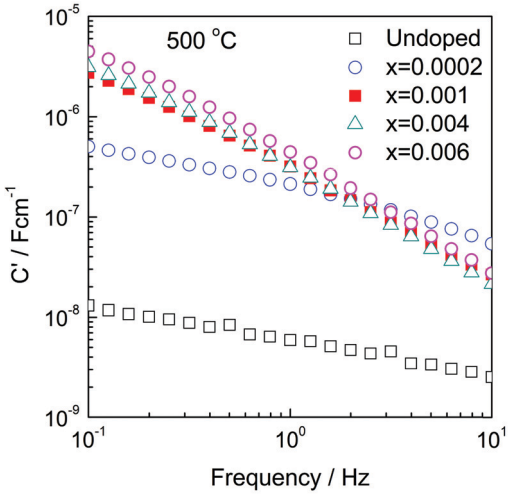

Fig. 7 C' spectroscopic plots for undoped rutile, x = 0.0002, 0.001, 0.004 and 0.006 at 500 °C.

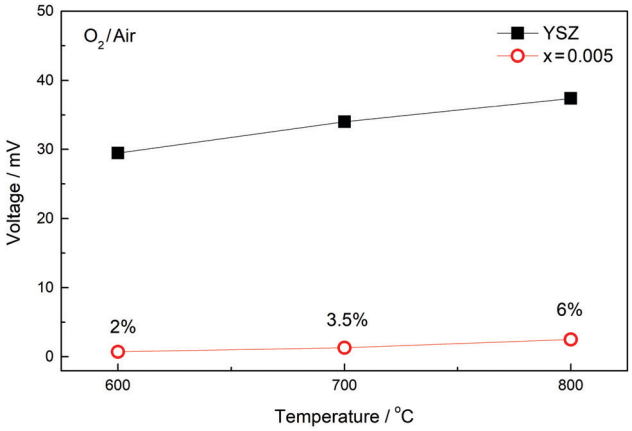

Fig. 8 EMF measurement of composition x = 0.005 at various temperatures; data for YSZ are also shown.

electromotive force, EMF, measurements of an oxygen concentration cell containing a sample confirm that any ionic conductivity is due to oxide ions. Third, variation of conductivity with pO_2 provides evidence of extrinsic semi-conductivity and enables the distinction between n- and p-type carriers generated by sample-atmosphere oxygen exchange reactions. Results from these three types of measurement are as follows.

First, C' data for some low x compositions are shown in Fig. 7. We interpret their magnitude, which increases with increasing x in the range 0.0002–0.006 and with decreasing frequency, to indicate a certain amount of ionic conduction. For materials that are exclusively ionic conductors, a double layer capacitor is created at the sample–electrode interface whose magnitude depends on contact area and sample–electrode separation with typical value around 1×10^{-5} F cm^{-1}. On the other hand, for conduction that is exclusively electronic, the contact capacitances are small, associated instead with the rough nature of sample–electrode interfaces and double layer capacitance phenomena are not seen in impedance data.

For sample x = 0.0002, the C' values, *e.g.*, 500 nF at 0.1 Hz, Fig. 7, are attributed to a combination of a double layer capacitor in parallel with an electronic pathway across the sample–electrode interface. This value of C' increases with x to reach a maximum of ~5 μF for x = 0.006 and continues with a high value through composition x = 0.008. For higher x values, however, C' decreases, but is still high in *e.g.*, x = 0.02 at 300 °C, Fig. S10(c) (ESI†). At these high x compositions, the materials show increased electronic conductivity, Fig. 10, leading to reduction in the effective transport number of oxide ions and significance of the blocking double layer capacitance.

The initial conclusion, therefore, is that the Cr-doped rutile samples are mixed conductors in which the oxide ion component arises as a consequence of the mechanism of Cr doping which involves oxygen vacancy creation, mechanisms (2)–(4). Both regions τ_1 and τ_2 are mixed conductors, but the transport numbers are composition-dependent.

Second, confirmation that the ionically conducting component in regions τ_1 and τ_2 is due to oxide ions was obtained from EMF measurements over the temperature range 600–800 °C for a cell that had air and O_2 in contact with opposite faces of a pellet of x = 0.005; EMF data are compared with those for YSZ in Fig. 8, from which approximate oxide ion transport numbers in the range 0.02–0.06 were obtained. These transport numbers should be treated with care since the sample of x = 0.005 contained both regions τ_1 and τ_2 whose transport numbers are likely to be different, as well as the grain boundary region, τ_3 and therefore, the transport data may depend on sample microstructure as well as composition. There is also the possibility of some residual porosity, either in the 90% dense ceramic, or associated with the seals, that may act to reduce the oxide ion transport numbers.

Third, impedance measurements in atmospheres of different pO_2 showed clear evidence of electronic conductivity, both n-type and p-type, depending on composition:

(a) In undoped rutile, the electronic conduction is primarily n-type. Impedance measurements showed a decrease in resistance with decreasing pO_2, in the sequence: O_2 → air → N_2, Fig. 9(a). This is attributed to loss of O_2 from sample surfaces and release of electrons according to:

$$2O^{2-} \leftrightarrow O_2 + 4e' \qquad (12)$$

The n-type behaviour is caused by a slight oxygen deficiency, $TiO_{2-\delta}$, formula (3), that arises during processing at high temperatures and is followed by incomplete oxygen uptake on subsequent cooling. Measurements were made at three pO_2 values, one of which, in N_2, is a rough estimate only; total conductivities are given in Fig. 9(a), inset. The data match approximately the expected slope of −1/4 which is the ideal behaviour in the n-type region, shown schematically in (i).

(b) With x = 0.0002, Fig. 9(b), impedance data show almost no dependence on pO_2, but with increasing x: 0.002 (c), 0.005 (d) and 0.01 (e), the data show p-type behaviour in which the resistance decreases with increasing pO_2. In such cases, holes are created by the absorption and dissociation/ionisation of

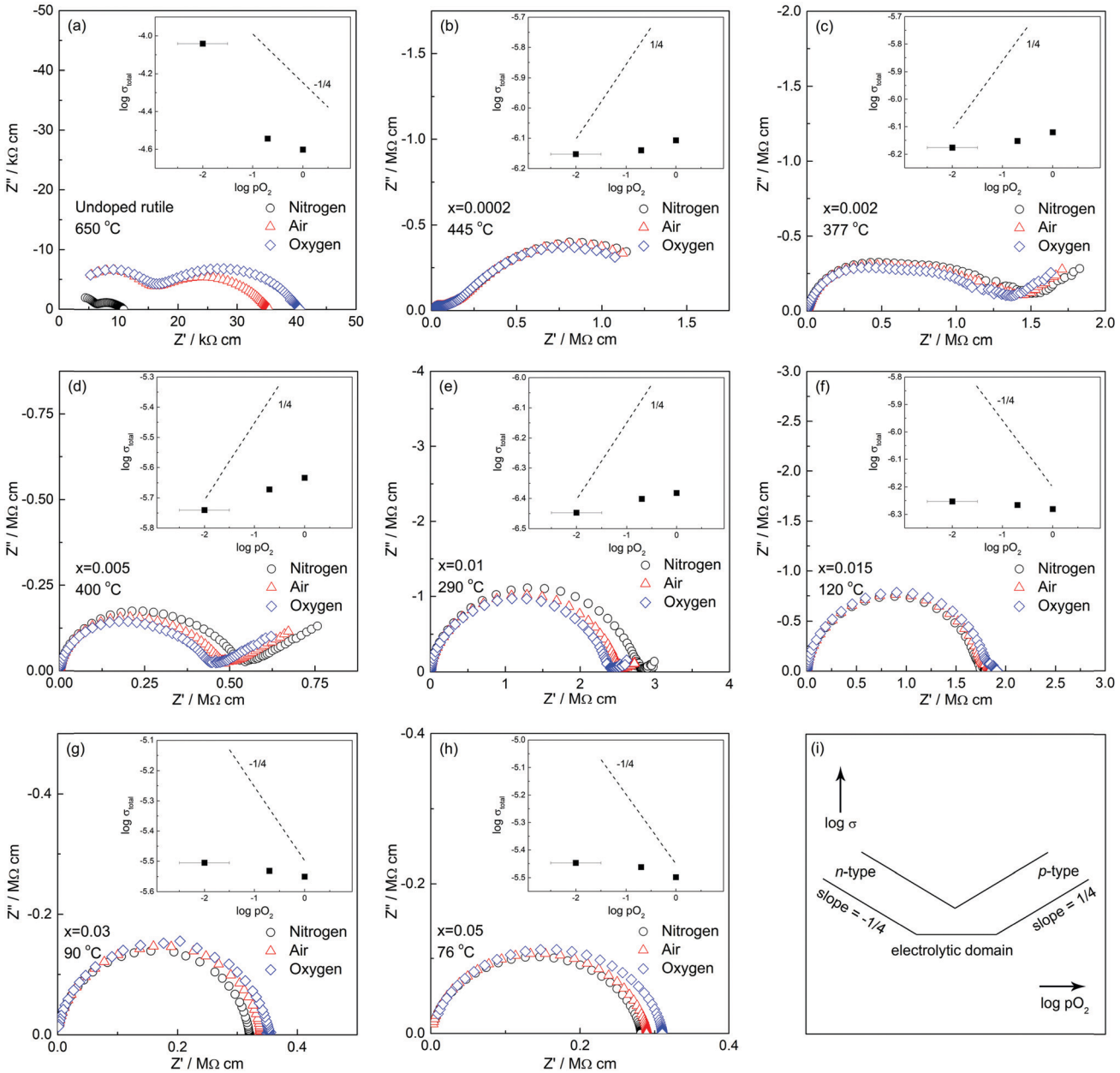

Fig. 9 (a–h) Effect of atmosphere on the impedance of pure and Cr-doped TiO_2 and (i) schematic dependence of conductivity on atmosphere.

oxygen molecules, eqn (7). The system is then in the p-type domain, (i), with a slope, ideally, of +1/4; the evidence for p-type behaviour is seen most clearly in (d) for x = 0.005. This pO_2 dependence refers to the total sample resistance. It clearly applies to region τ_2 but is not known whether it also applies to the grain cores, τ_1.

(c) At still higher x: 0.015 (f), 0.03 (g) and 0.05 (h), the behaviour appears to return to n-type but the variation with pO_2 is small, unlike that shown by undoped rutile, and may therefore have a different explanation.

The data shown in Fig. 9 cover a wide range of Cr contents but also a wide range or measuring temperatures. In this discussion, we focus on the pO_2-dependence but recognise that a more extensive study of the effect of temperature is required to obtain a complete picture of the transition between the different conductivity regimes and also to separate the behaviour of regions τ_1 and τ_2.

The remarkable transition from n-type to p-type conductivity with increasing Cr content may be rationalised as follows. Undoped rutile is, as-expected, n-type if there is a residual deficiency of oxygen in the samples after sintering, Fig. 9(a). The dramatic rise in electronic conductivity of region τ_1 on addition of Cr^{3+} was, however, unexpected: the conductivity σ_1 at very low x is many orders of magnitude higher than that of undoped rutile prepared under the same conditions and has much smaller activation energy, Fig. 10(b). It is attributed to

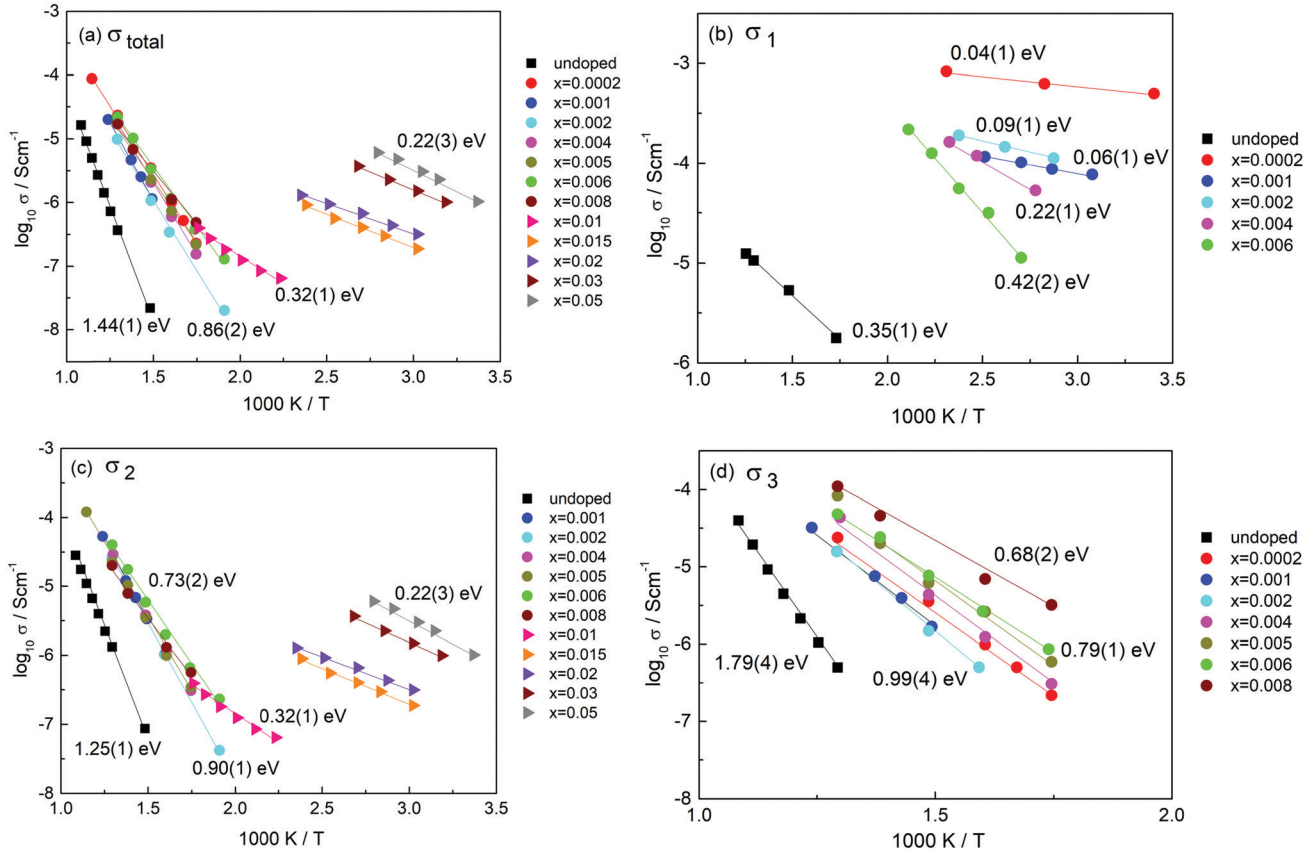

Fig. 10 Arrhenius plots of (a) σ_{total}, (b) σ_1, (c) σ_2 and (d) σ_3.

double doping by Ti^{3+} and Cr^{3+} and therefore, to a large increase in n-type electron content associated with the Ti^{3+} ions.

As a consequence of doping Cr^{3+} and Ti^{3+} into the rutile lattice, the number of oxygen vacancies exceeds greatly the number associated with oxygen loss at high temperatures. Under these conditions, the defect equilibria associated with oxygen loss from un-doped rutile are modified by the additional mechanism, associated with the co-dopant Ti^{3+} ions, that controls both the oxygen vacancy content and the electron content. The n-type conductivity and probably the Ti^{3+} content, pass through a maximum around $x = 0.0002$. At higher x, the oxygen vacancy content increases further, but (i) the Ti^{3+} content decreases and (ii) there is increasing absorption of atmospheric oxygen by the vacancies giving rise to holes on oxygen, eqn (7). Consequently, there is a gradual change from n-type behaviour associated with the decreasing number of Ti^{3+} ions to p-type behaviour associated with the increasing number of O^- ions. It is quite common for materials that have oxygen vacancies to absorb O_2 and show p-type conductivity.[16,21] We do not know whether this is a major equilibrium reaction at high temperatures or is promoted by oxygen uptake during cooling.

The electronic conductivity that results is therefore a combination of n-type conduction associated with the residual Ti^{3+} content and hole conductivity associated with O^-. No pO_2 dependence is seen for $x = 0.0002$ but this may be because σ_1 is too high, $\leq 10^{-3}$ S cm^{-1} to be sensitive to small changes in electron concentration caused by changes in pO_2 at sample surfaces. For x in the range, 0.002 to 0.01, the value of σ_1 decreases significantly, Fig. 10(b), but also the volume fraction of region τ_1 decreases and at the same time, that of τ_2 increases, Fig. 4(c) and 5. Regions τ_2 and τ_3 dominate the impedance data for this composition range and the pO_2-dependence indicates that these regions are p-type, Fig. 9.

3.2.4 Conductivity Arrhenius plots. Conductivity data for τ_1, τ_2 and τ_3 as well as total conductivities were estimated variously from M'' peak maxima (τ_1) and Z^* plots (τ_2, τ_3, total conductivity). The four sets of conductivities for all compositions over which data could be obtained are summarised in Fig. 10.

Data for σ_1 are shown in (b); these cover the composition range below $x = 0.01$ since component τ_1 is not detected at higher Cr contents. The conductivity is greatest and the activation energy least for the composition with the lowest Cr content, $x = 0.0002$. The values of the Arrhenius parameters change systematically with increasing x: conductivity decreases and activation energy increases.

These doped conductivities, σ_1 are all very much greater than that of un-doped rutile pellets prepared under the same conditions, (b). The conductivity of undoped rutile is extremely sensitive to oxygen loss and the associated presence of Ti^{3+} ions, as shown by samples quenched from different

temperatures whose conductivity can vary by many orders of magnitude.[7] The activation energy is also a good indicator of oxygen deficiency, although a quantitative scale of activation energy *vs.* δ has not been established. The value of 0.35(1) eV for undoped rutile, (b), is similar to what would be expected for a sample quenched after heating in air at 800 °C.[7] Since the rutile pellet used here was furnace-cooled after sintering at 1350 °C, it appears that the pellet core, τ_1, had maintained equilibrium with the furnace atmosphere down to ~800 °C but that a residual oxygen deficiency remained in the pellets at the end of the cooling cycle.

We attribute the dramatic increase in conductivity of component τ_1 for x = 0.0002, (b), to the presence of Ti^{3+} as a co-dopant on Cr doping. The condition that $2x = \delta$ applies at very low x because each substitutional Cr^{3+} ion requires one associated Ti^{3+} ion in order to charge-compensate for one oxygen vacancy. As x increases beyond 0.0002, δ becomes increasingly smaller than x as the mechanism gradually changes to (2) until finally, $\delta = 0$ at $x = \sim 0.01$; at this point there appears to be no Ti^{3+} co-dopant present. If we regard the conduction electrons associated with Ti^{3+} as polarons, the polaron size may decrease with x at the same time as their number decreases, thus accounting for both the decrease in conductivity and increase in activation energy with increasing x.

Conductivity data for σ_2 are shown in Fig. 10(c). For the low x compositions, 0.001–0.008, data are similar with activation energy in the range 0.73(2) to 0.90(1) eV. The general similarity in the data for σ_{total} and σ_2, a and c, indicates that region τ_2 controls the overall impedance for most compositions. An abrupt change occurs between x = 0.008 and 0.01, at which point σ_2 becomes the main bulk conductivity and has values that increase with x although all have a similar, small activation energy of ~0.25 eV. Composition x = 0.01 is at the cross-over between the low x and high x conductivity regimes for σ_2, which are characterised by activation energies of approximately 0.73 and 0.22 eV, respectively. In the low x range, it appears that conductivity σ_2 is a mixture of p-type and ionic although the ionic conductivity component may not be high enough to impact significantly the measured values and activation energy.

For the high x compositions, conduction is also mixed, but appears to change from p-type to n-type around x = 0.01–0.015, Fig. 9; some residual oxide ion conductivity is still seen at x = 0.02, as shown by high capacitance at low frequency and high temperature in Fig. S10(c) (ESI†). The constancy of the activation energy of σ_2 for different compositions in the high x region implies a single predominant conduction mechanism, in which an increase in carrier concentration is responsible for the increase in conductivity with increasing x. We therefore attribute this to a mechanism associated with the Cr^{3+} ions. The variation of conductivity with atmosphere in this region may arise because some of the O^- ions absorbed by oxygen vacancies desorb with decreasing pO_2, giving rise to apparent n-type conductivity, but from the small dependence of conductivity on pO_2 shown in Fig. 9(f–h), this is not the main source of the conductivity; further work is required to understand that result.

Conductivity data for σ_3 are shown in Fig. 10(d). There is a gradual increase in conductivity with x, although the data for x = 0.0002 are somewhat out of line with this trend. From its capacitance value, τ_3 appears to be a grain boundary component that has significant ionic conductivity since region τ_3 is not seen for high x compositions which are mainly electronic conductors. The activation energy for τ_3 is in the range 0.68(2) to 0.99(4) eV and probably represents mixed conductivity. The similarity in conductivities and activation energies of τ_2 and τ_3, such as shown in Fig. 4(f), indicates a strong similarity in the nature of the two regions; possibly, τ_3 represents a constriction impedance between grains in samples that are not fully dense;[22] alternatively, it may be due to a space charge layer that develops if there is an in-balance between defect distributions throughout the τ_2 grains.

3.2.5 Electrical microstructures. The electrical properties of low x compositions, as shown especially by the presence of double peaks in the M'' spectra, Fig. 4(c) and 5, indicate a two-phase electrical microstructure. The relative amount of the two components changes systematically with x. One component, identified as τ_1 has a composition very close to TiO_2, $x \leq 0.0002$, with a small, but essential amount of Cr and has high electronic conductivity attributed to the presence of Ti^{3+} ions. The Ti^{3+} ions form in response to the need to maintain local electro-neutrality.

The second component, τ_2 has composition x = 0.009(1) and has a more modest level of semi-conductivity compared to component τ_1. Electrically, τ_2 with composition x = 0.009(1) is the end-member of a range of homogeneous solid solutions extending to x = 0.05 and perhaps beyond whose conductivity is controlled by the Cr content and is mainly electronic with a small amount of oxide ion conductivity. Composition x = 0.009(1) represents the composition at which there is sufficient Cr^{3+} present to avoid the need for the additional double substitution mechanism of charge compensation; it corresponds to substitution of ~1% of the Cr acceptor dopant into the rutile structure.

For the range of compositions $0.0002 \leq x \leq 0.009$, the impedance data and the equivalent electrical circuit, Fig. 3 that represents the data, indicate that τ_1 and τ_2 are in series. This is especially clear since the conductivity of τ_1 is many orders of magnitude greater than that of τ_2 and therefore, there is no percolation conduction pathway through regions τ_1 alone. The conclusion is that, in this composition range, a core–shell structure exists with a highly conducting grain core, τ_1 surrounded by a resistive shell, τ_2. The relative thicknesses of core and shell regions depend on composition x. Region τ_3 is identified as either a typical grain boundary or a space charge layer from the magnitude of its capacitance and appears to be a modest conductor of oxide ions and p-type electrons.

There is no evidence that the region $0.0002 \leq x \leq 0.009$ is a traditional two-phase region in which the two components have the specified end-member compositions. Thus, there is no evidence of Cr segregation from the TEM results and therefore, the Cr contents appear be the same in core and shell regions for a given sample. Instead, the two components may be

distinguished by their mechanism of charge compensation. This also accounts for the variation with x of conductivity and activation energy for region τ_1 with the implication that the composition of τ_1 changes although it is in a region that, electrically, is two-phase.

4 Conclusions

Synthesis of Cr-doped rutile was carried out by solid state reaction. A single-phase product with general formula, $Ti_{1-x}Cr_xO_{2-x/2-\delta}$ with homogeneous distribution of Cr was obtained; the synthesis may have been facilitated by vapour phase transport of Cr with volatile CrO_3 as a transporting agent.

The defect structure and electrical properties of Cr-doped rutile are remarkably dependent on composition. Lattice parameters show very non-linear composition-dependence. The main substitution mechanism involves oxygen vacancy creation, but to achieve local charge balance, each oxygen vacancy requires two trivalent acceptor dopants. At very low Cr contents, the statistical distribution of Cr^{3+} ions does not allow two Cr^{3+} ions to be present near each oxygen vacancy; instead, it is proposed that Ti^{3+} acts as an additional acceptor dopant, even though Ti^{3+} ions are not expected to be present under oxidising synthesis conditions. There are two variables in the expanded formula, $Ti_{1-x-2\delta}{}^{4+}Cr_x{}^{3+}Ti_{2\delta}{}^{3+}O_{2-\frac{x}{2}-\delta}$, the Cr content, x and oxygen loss, δ associated with Ti^{3+} ions. At the lowest x studied, 0.0002, ideally $\delta = 2x$, but with increasing x, δ decreases and is zero for $x \geq 0.009$. The unit cell volume passes through a maximum at $x \sim 0.005$, attributed to the presence of large, co-doped Ti^{3+} ions and is superposed on a more gradual increase associated with oxygen vacancy creation and weakening of the Ti,Cr–O bond strength.

For low x compositions, $0.0002 \leq x \leq 0.008$, the materials are electrically heterogeneous and consist of two regions of approximate composition 0.0002 and 0.009. These regions appear not to be classic two-phase in nature but instead refer to regions where the two charge compensation mechanisms, involving co-doping by Cr^{3+}, Ti^{3+} in region τ_1 and doping by Cr^{3+} alone in region τ_2, predominate, both of which involve oxygen vacancy creation for charge balance. The conductivity of the main, low x bulk component, σ_1 was a maximum for the composition with the smallest Cr content that was studied, x = 0.0002; with increasing x, σ_1 decreased and activation energy increased, but the volume fraction of τ_1 also decreased; τ_1 was not seen at all in high x compositions.

Two types of electronic conductivity were observed and included a remarkable switch from n-type to p-type conductivity with increasing x. First, n-type behaviour in undoped rutile is associated with a small oxygen deficiency introduced during sintering which was not fully regained during cooling. This n-type conductivity increases greatly with small x, 0.0002 and is associated primarily with co-doped Ti^{3+} ions. Second, at higher x, as the extent of co-doping by Ti^{3+} and Cr^{3+} decreases, but oxygen vacancies continue to be created, p-type behaviour was observed. This is attributed to the absorption of oxygen, ionisation of under-bonded O^{2-} ions located near to Cr^{3+} acceptor dopants and hole location on oxide ions. As well as p-type conductivity, oxide ion conductivity associated with oxygen vacancies is observed, giving rise to a range of compositions that show mixed p-type and oxide ion conductivity.

The compositional limit of co-doping with two acceptors, Cr^{3+} and Ti^{3+} appears to be $x \leq 0.009(1)$. For compositions with $x > 0.01$, the materials are electrically homogeneous and have only one electrical component that shows composition-dependent conductivity, attributed to hopping electrons associated with the Cr^{3+} dopant. A limited amount of oxide ion conductivity still occurs, but conduction is mainly electronic.

We see no evidence for CS planar defects for compositions $x \leq 0.03$.

Author contributions

ARW conceived and planned the project, YD synthesised the materials, characterised them by XRD and made the impedance measurements. XLP, HW and BY did the electron microscopy with guidance from HYW. All authors contributed to discussion of the results. ARW with input from YD contributed the main conclusions of the work. All authors reviewed and approved the final version of the manuscript.

Conflicts of interest

The authors declare no conflicts of interest.

Acknowledgements

X. P., Han W., B. Y. and H. W. would like to acknowledge the support from the U.S. Office of Naval Research (Contract numbers: N00014-17-1-2087 and N00014-20-1-2043) for the TEM work at Purdue University.

References

1 J. Nowotny, M. Alim, T. Bak, M. Idris, M. Ionescu, K. Prince, M. Sahdan, K. Sopian, M. Teridi and W. Sigmund, *Chem. Soc. Rev.*, 2015, **44**, 8424–8442.
2 K. Rahman, T. Bak, A. Atanacio, M. Ionescu and J. Nowotny, *Ionics*, 2018, **24**, 309–325.
3 X. Li, Z. Guo and T. He, *Phys. Chem. Chem. Phys.*, 2013, **15**, 20037–20045.
4 A. Stoneham and P. Durham, *J. Phys. Chem. Solids*, 1973, **34**, 2127–2135.
5 M. Blanchin, P. Faisant, C. Picard, M. Ezzo and G. Fontaine, *Phys. Status Solidi A*, 1980, **60**, 357–364.
6 R. Gibb and J. Anderson, *J. Solid State Chem.*, 1972, **4**, 379–390.
7 Y. Liu and A. R. West, *J. Am. Ceram. Soc.*, 2013, **96**, 218–222.
8 M. Nowotny, T. Bak and J. Nowotny, *J. Phys. Chem. B*, 2006, **110**, 16270–16282.

9 Y. Dang and A. R. West, *J. Am. Ceram. Soc.*, 2019, **102**, 251–259.
10 S. Somiya, S. Hirano and S. Kamiya, *J. Solid State Chem.*, 1978, **25**, 273–284.
11 H. D. Werner, *Neues Jahrb. Mineral. Mh.*, 1974, **5**, 218–234.
12 S. Andersson, A. Sundholm and A. Magnéli, *Acta Chem. Scand.*, 1959, **13**, 989–997.
13 D. K. Philp and L. Bursill, *J. Solid State Chem.*, 1974, **10**, 357–370.
14 M. Binnewies, R. Glaum, M. Schmidt and P. Schmidt, *Z. Anorg. Allg. Chem.*, 2013, **639**, 219–229.
15 P. Ren, N. Masó and A. R. West, *Phys. Chem. Chem. Phys.*, 2013, **15**, 20943–20950.
16 P. Ren, N. Masó, Y. Liu, L. Ma, H. Fan and A. R. West, *J. Mater. Chem. C*, 2013, **1**, 2426–2432.
17 M. Castellanos and A. R. West, *J. Chem. Soc., Faraday Trans. 1*, 1980, **76**, 2159–2169.
18 S. R. Bishop, K. L. Duncan and E. D. Wachsman, *Electrochim. Acta*, 2009, **54**, 1436–1443.
19 S. Grieshammer and M. Martin, *J. Mater. Chem. A*, 2017, **5**, 9241.
20 A. R. West, D. C. Sinclair and N. Hirose, *J. Electroceram.*, 1997, **1**, 65–71.
21 N. Masó and A. R. West, *Chem. Mater.*, 2012, **24**, 2127–2132.
22 P. G. Bruce and A. R. West, *J. Solid State Chem.*, 1982, **44**, 354–365.

